

Maximum Likelihood Motion Estimation in 3D Echocardiography through Non-rigid Registration in Spherical Coordinates

Andriy Myronenko¹, Xubo Song¹, and David J. Sahn²

Department of Science and Engineering, School of Medicine¹
Cardiac Fluid Dynamics and Imaging Laboratory²
Oregon Health and Science University^{1,2}

20000 NW Walker Road, Beaverton, OR 97006, USA

myron@csee.ogi.edu, xubosong@csee.ogi.edu, sahnd@ohsu.edu

Abstract. Automated motion tracking of the myocardium from 3D echocardiography provides insight into heart’s architecture and function. We present a method for 3D cardiac motion tracking using non-rigid image registration. Our contribution is two-fold. We introduce a new similarity measure derived from a maximum likelihood perspective taking into account physical properties of ultrasound image acquisition and formation. Second, we use envelope-detected 3D echo images in the raw spherical coordinates format, which preserves speckle statistics and represents a compromise between signal detail and data complexity. We derive mechanical measures such as strain and twist, and validate using sonomicrometry in open-chest piglets. The results demonstrate the accuracy and feasibility of our method for studying cardiac motion.

1 Introduction

Quantitative analysis of 3D echo images can provide mechanical measurements such as strain, wall thickening, twist, volume and ejection fraction, which can be used to evaluate the elasticity and contractility of the myocardium [1]. In this paper, we describe a method to estimate the myocardial motion, from 3D ultrasound image sequence. The idea is to consecutively align 3D images one onto another and track the motion field using non-rigid image registration [2, 3]. Spatially-dense displacement field can be derived, from which we compute quantitative measures such as strain and twist.

Applications of non-rigid image registration for quantitative analysis from 3D echocardiography have been recently proposed by several researchers including Elen et al. [3], Leung et al. [4], Ledesma-Carbayo et al. [5] and Sanchez-Ortiz et al. [6]. Despite significant algorithmic advances, registration of 3D ultrasound images remains challenging due to multiple intensity artifacts, low image quality, speckle and large computation load.

The novelty of this paper is two-fold. First, we introduce a new similarity measure for ultrasound image registration. We derive it from a maximum likelihood (ML) perspective taking into account the physical properties of ultrasound

image acquisition and formation. Second, we use envelope-detected 3D echo images in the raw *spherical coordinates* format, which preserves speckle statistics and represents a compromise between signal detail and data complexity. We validate the algorithm-derived measures to those derived from sonomicrometry on open chest pigs.

Maximum likelihood approach: Registration of 3D echocardiogram has several specifics compared to general non-rigid registration techniques, which can be taken into account using the ML approach. Cohen and Dinstein [7] derived a CD_2 similarity measure using the ML approach. They assumed that two consecutive ultrasound images are both corrupted by multiplicative noise with Rayleigh pdf and that noise pdfs are independent of each other.

Here, we derive a new similarity measure assuming that Rayleigh noise in consecutive images is correlated and that speckle is blurred. The speckle noise is a random signal, but has implicit dependence on the underlying imaging object structure. If the static object is imaged twice, the speckle remains the same [8]. This is in contrast to other noise sources, e.g. electrical noise, which always has a random nature. Several researchers showed the dependence of speckle correlation on the motion of imaged area [9, 10]. If two consecutive images are taken with sufficiently high frame rate, which is the case for modern ultrasound devices, the speckle noise formation between the consecutive frames is similar, and two speckle noise variables are correlated [8]. Finally, during data acquisition, the speckle is not measured at an ideal point, but rather integrated over some area of detector element. The speckle pattern motion, caused by imaging area motion, makes the measurement quantity integrated over some part of ideal speckle pattern. This results in *blurred speckle* effect, which modifies the density function [11].

Spherical coordinates: A typical digital ultrasound processing chain consists of the following four steps: 1) Multiple analog-to-digital converters convert the analog radio frequency (RF) signal from the ultrasound transducer to a digital RF signal; 2) Beamforming is applied to individual RF signals by applying time delays and summations as a function of time and transformed into a single RF signal, which is often called “beamformed RF” data; 3) The RF signal is filtered, is run through an envelope detector and is log compressed into a gray scale format. At this stage the data is represented as a sequence of 3D arrays, each of which is a 3D image in the raw spherical coordinate system; 4) Finally, the envelope-detected signal is scan converted to Cartesian coordinate system and interpolated at the regular grid to form the digital 3D image (also called B-mode data). The data corresponding to the third and fourth steps (spherical vs. Cartesian coordinates of post-converted image) is shown in Figure 1.

We shall use envelope-detected 3D echo image in the raw spherical coordinates (step 3), before the final conversion to the Cartesian coordinates. In other words, we take one step back in 3D echo image formation. We note that our approach differs significantly from the registration methods [12] that build a spherical or cylindrical transformation model along the heart orientation axis, using

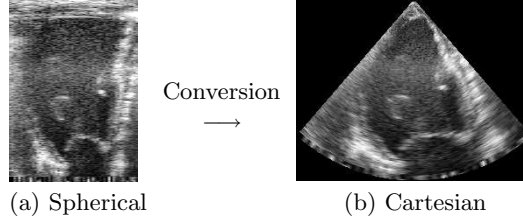


Fig. 1. (a) An example of spherical data displayed as a 2D array ($416 \times 62 \times 56$). (b) The spherical data is converted to the Cartesian data ($208 \times 297 \times 269$).

Cartesian post-converted images (step 4). Whereas, we use envelope-detected images in raw spherical coordinates (step 3), which may or may not be in alignment with heart orientation.

The main benefits of using envelope-detected image in spherical coordinates, in contrast to the final Cartesian coordinates, is the preservation of speckle statistics and avoidance of information loss associated with scan conversion and interpolation. The envelope-detected data has higher resolution in vicinity of transducer and lower resolution away from the transducer. Also, the axial resolution is much higher than the lateral. After conversion to the Cartesian system some information is lost, including high axial resolution and high resolution closer to the transducer, and additional errors are introduced, for instance, the new voxels that appear after regular grid interpolation in the areas far from the transducer. Even though the envelope-detected data in spherical coordinates still contains less information than RF data, it represents a reasonable compromise between level of the signal details and computational complexity.

2 Maximum Likelihood Motion Estimation

Consider two 3D ultrasound images I and J acquired at consecutive time instances. The maximum likelihood (ML) approach to estimate the transformation \mathcal{T} between the images is to maximize the conditional probability [7, 13], $p(J(\mathcal{T})|I, \mathcal{T})$, or equivalently minimize the following energy function

$$E(\mathcal{T}) = \sum_{n=1}^N -\log p(J_n(\mathcal{T})|I_n, \mathcal{T}) \quad (1)$$

where we assumed that all voxelwise conditional probabilities are i.i.d. and $J_n(\mathcal{T})$ denotes the intensity values of n^{th} voxel after applying the transformation \mathcal{T} .

In ultrasound imaging, the image intensities are the log-compressed values of the envelope amplitudes (denoted as a and b) [8]:

$$I_n = D \log(a) + G; \quad J_n(\mathcal{T}) = D \log(b) + G \quad (2)$$

where G and D are the linear gain and the dynamic range constants.

When the speckle is fully developed the noise is multiplicative and follows the Rayleigh pdf [8, 11]:

$$p(n) = \frac{n}{\sigma^2} \exp \frac{-n^2}{2\sigma^2}, \quad n \geq 0 \quad (3)$$

If $a = sn_1$ and $b = sn_2$ are the realizations of the informative signal s corrupted by multiplicative Rayleigh noise n_1 and n_2 respectively, and $\eta = \frac{n_1}{n_2}$ is the division of two random variables [14], then

$$p(J_n(\mathcal{T})|I_n, \mathcal{T}) = \frac{\eta}{D} p(\eta) = \frac{\eta}{D} \int n_2 p(\eta n_2, n_2) dn_2 \quad (4)$$

2.1 Independent Rayleigh Noise Assumption

Cohen and Dinstein [7] assumed that the noise at consecutive ultrasound images is independent and has equal variances, then $p(J_n(\mathcal{T})|I_n, \mathcal{T}) = \frac{1}{D} \frac{2\eta^2}{(\eta^2+1)^2}$ and the similarity function takes the form¹

$$E(\mathcal{T}) = \sum_{n=1}^N -\log \frac{e^{2d_n}}{(e^{2d_n} + 1)^2} + \text{const}; \quad d_n = \frac{J_n(\mathcal{T}) - I_n}{D} \quad (5)$$

where by d_n we defined a scaled difference between the intensities of corresponding image voxels. Cohen and Dinstein derived this similarity function and called it CD_2 similarity measure². This similarity measure showed superior performance comparing to other similarity measure for ultrasound image tracking, and was widely used in tracing and block matching algorithms [15–18].

2.2 Correlated Rayleigh Noise Assumption

Here we do not assume that Rayleigh noise n_1 and n_2 are independent. If two consecutive images I and J are taken with sufficiently high frame rate, which is the case for modern ultrasound devices, the speckle noise formation between the consecutive frames is similar, and the random variables n_1 and n_2 are correlated [8]. The bivariate Rayleigh distribution [11] of two random variable n_1 and n_2 with equal variance σ^2 is

$$p(n_1, n_2) = \frac{n_1 n_2}{(1-\rho)\sigma^4} e^{-\frac{n_1^2 + n_2^2}{2\sigma^2(1-\rho)}} I_0 \left[\frac{\sqrt{\rho} n_1 n_2}{(1-\rho)\sigma^2} \right]; \quad I_0(z) = \sum_{k=0}^{\infty} \frac{z^{2k}}{2^{2k}(k!)^2} \quad (6)$$

¹ Usually, the ultrasound log-compression is done with decimal logarithm function, which results in $10^{2d_n} = e^{2d_n \ln 10}$ terms instead of e^{2d_n} . We absorb the scaling $\ln 10$ into the constant D for convenience.

² In its original derivation, Cohen and Dinstein do not account for scaling constant D , which is equivalent to assume $D = 1$.

where I_0 is a modified Bessel function of the first kind with zero order, $0 \leq \rho < 1$ is a correlation coefficient and $n_1 \geq 0$, $n_2 \geq 0$. Substitution Eq. 6 in Eq. 4, we have to take a non-trivial integral

$$p(\eta) = \int_0^\infty n_2 p(\eta n_2, n_2) dn_2 = \int_0^\infty \frac{\eta n_2^3}{(1-\rho)\sigma^4} e^{-\frac{n_2^2(1+\eta^2)}{2\sigma^2(1-\rho)}} \cdot I_0\left(\frac{\sqrt{\rho}\eta n_2^2}{(1-\rho)\sigma^2}\right) dn_2 = \frac{2(1-\rho)\eta}{(1+\eta^2)^2} \sum_{k=0}^\infty \left(\frac{\eta^2\rho}{(1+\eta^2)^2}\right)^k \frac{(2k+1)!}{(k!)^2} = \frac{2(1-\rho)\eta}{(1+\eta^2)^2} \left(1 - \frac{4\rho\eta^2}{(1+\eta^2)^2}\right)^{-\frac{3}{2}} \quad (7)$$

To simplify, we exchanged the integration and summation and used the formula for integration of definite integrals and for infinite series summation [19] (for $m = 1$):

$$\sum_{k=0}^\infty z^k \frac{(2k+2m-1)!}{(k+m-1)k!} = \frac{(2m-1)!}{(m-1)!} (1-4z)^{-\frac{2m+1}{2}} \quad (8)$$

Thus the new similarity function takes the form

$$E(T) = \sum_{n=1}^N -\log \frac{e^{2d_n}}{(e^{2d_n} + 1)^2} + \frac{3}{2} \log\left(1 - \frac{4\rho e^{2d_n}}{(e^{2d_n} + 1)^2}\right) = \sum_{n=1}^N \frac{3}{2} \log(\cosh^2(d_n) - \rho) - \frac{1}{2} \log(\cosh^2(d_n)) + \text{const} \quad (9)$$

By convention, we shall call this similarity function *MS* similarity measure. As a check on this result, if the correlation coefficient $\rho = 0$, then *MS* simplifies to *CD*₂ in Equation 5.

2.3 Blurred Speckle

The probability density function of speckle noise at an ideal point in space is quite idealistic. During data acquisition, the speckle is not measured at an ideal point, but rather integrated over some area of detector element. Also, the speckle pattern motion, caused by imaging area motion, makes the measurement quantity integrated over some part of ideal speckle pattern. This results in *blurred speckle* effect, which modifies the density function [11]. To deal with the problem in optical imaging, Goodman [11] showed that a Gamma density is a good approximation to speckle intensity pdf. In ultrasound imaging, the detector is pressure sensitive, which means that we measure the amplitude (square root of intensity). Using a change of variable for the Gamma pdf, we achieved that the blurred speckle has a Nakagami distribution

$$p(n) = \frac{m^m}{2^{m-1}\sigma^{2m}\Gamma(m)} n^{2m-1} e^{-\frac{mn^2}{2\sigma^2}}, \quad n > 0 \quad (10)$$

which is also called a generalized Rayleigh distribution [20]. For $m = 1$ the distribution reduces to the Rayleigh distribution (Eq. 3). The application of the Nakagami distribution in ultrasound imaging has been popularized by Shankar [21].

He showed that the Nakagami distribution fits the real speckle distribution superior to Rayleigh and K-distributions.

We assume that two speckle variables are correlated, and their joint pdf is a bivariate Nakagami distribution [22]

$$p(n_1, n_2) = \frac{m^{m+1}(n_1 n_2)^m}{2^{m-1} \sigma^{2(m+1)} (1-\rho) \rho^{\frac{m-1}{2}} \Gamma(m)} e^{-\frac{m(n_1^2 + n_2^2)}{2(1-\rho)\sigma^2}} I_{m-1} \left(\frac{m\sqrt{\rho} n_1 n_2}{(1-\rho)\sigma^2} \right) \quad (11)$$

Here, we assumed that the distribution widths σ^2 are equal, ρ is a squared correlation coefficient $0 \leq \rho < 1$ and I_{m-1} is a modified Bessel function of the first kind of order $m-1$. Substitution Eq. 11 in Eq. 4, we obtain

$$p(\eta) = 2(1-\rho)^m \frac{\Gamma(2m)}{\Gamma(m)^2} \frac{\eta^{2m-1}}{(\eta^2 + 1)^{2m}} \left(1 - \frac{4\rho\eta^2}{(1+\eta^2)^2} \right)^{-\frac{2m+1}{2}} \quad (12)$$

To simplify, we exchanged the integration and summation and used the formula for integration of definite integrals and for infinite series summation [19] (Eq. 8). Thus, the similarity function, based on blurred and correlated speckle assumptions, is

$$f = -m \log \frac{e^{2d}}{(e^{2d} + 1)^2} + \frac{2m+1}{2} \log \left(1 - \frac{4\rho e^{2d}}{(e^{2d} + 1)^2} \right) + const = \frac{2m+1}{2} \log(\cosh^2(d) - \rho) - \frac{1}{2} \log(\cosh^2(d)) + const. \quad (13)$$

which, we shall call the MS_2 similarity measure. As a check, for $m=1$, MS_2 simplifies to MS (Eq. 9).

2.4 Analysis of the CD_2 , MS and MS_2 Similarity Measures

The CD_2 similarity measure, we believe, is of general interest for image registration. We can rewrite the Eq. 5 in different but equivalent form as $E(T) \propto \sum_n -\log \text{sech}^2(d_n)$, where sech is a hyperbolic secant function. Thus, we could have achieved the same similarity measure by simply assuming an additive image noise with logistic pdf. The logistic distribution resembles the Gaussian distribution, but has heavier tails (higher kurtosis) and thus belongs to the class of super-gaussian distributions.

From the optimization perspective, we can analyze the shape of the voxel-wise similarity function and its derivative (influence function), rather than the distribution itself. The shape of CD_2 similarity function resembles the shape of the absolute value function (L_1 norm between the images), but is also differentiable at the origin. The derivative of the CD_2 function is \tanh , which approximates the step function. Figure 2(a,b) shows the plot of CD_2 similarity function and its derivative versus L_1 norm ones. L_1 norm belongs to the family of robust similarity measures with many applications in statistics, machine learning and computer vision areas. This supports the robust and accurate performance of CD_2 measure for image registration.

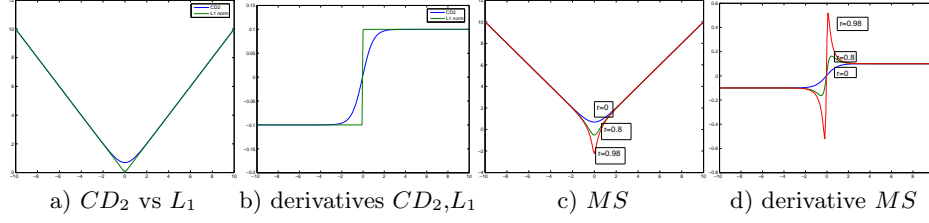


Fig. 2. The plot of CD_2 similarity function and its derivative versus L_1 norm function.

The MS similarity measure generalizes the CD_2 measure. Figure 2(c,d) shows the plot of MS similarity function and its derivative for different values of correlation coefficient ρ . For $\rho = 0$, the MS simplifies to CD_2 . For the larger values of correlation coefficient, MS has a sharper peak in a vicinity of the origin and otherwise asymptotically approaches the L_1 norm function. From the optimization perspective, the higher the correlation value, the higher weight is assigned to the closer intensity differences, which makes the similarity function more robust to outliers (large differences in intensity). Furthermore, the extra parameter m , in the MS_2 similarity measure, introduces a change of slopes compared to the MS ones, which adds a balance control on weights for closer and further intensity differences. The behavior of MS and MS_2 function becomes similar to the behavior of functions in the robust M-estimator approach. The robustness to outliers are crucial in registration of ultrasound images, which typically includes multiple intensity artifacts.

3 Validation by Sonomicrometry

Sonomicrometers implanted on open chest piglets were used for validation. An array of seven sonomicrometers (sono crystals) was implanted as two sets: three sonomicrometers at apex level and four sonomicrometers closer to the base level in the LV myocardium. Using Sonometrics software, we computed off-line the pair-wise crystal distances. From these distances, we computed pairwise strains and between-plane twist, which were used as ground truth for validation.

To compare strain and twist derived from the registration algorithm to those from the sonomicrometry, we visually located, based on anatomical markers, the sono crystals positions on the myocardium in the end diastole volume. These locations were propagated across time by the displacement field obtained from the nonrigid registration algorithm.

4 Results

We acquired the 3D echo sequences using Philips iE33 with EKG gating. Twenty different sequences were taken from 5 piglets. The animals were anesthetized

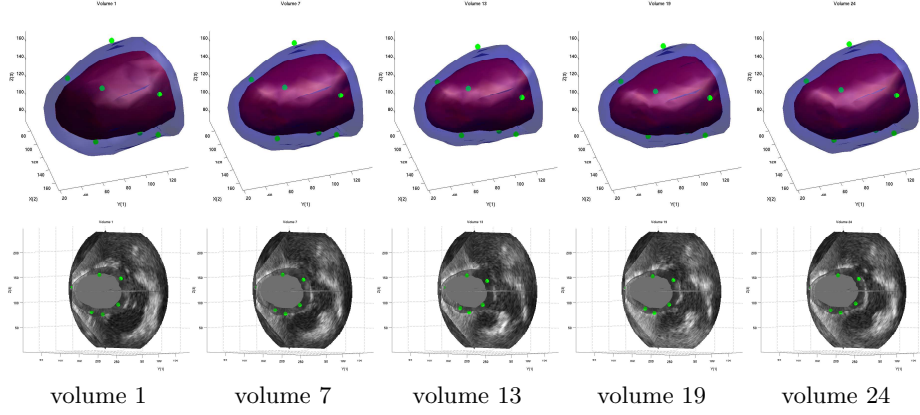


Fig. 3. The LV contour and sonomicrometer motion found during the cardiac cycle (24 consecutive volumes). LV achieves the maximum contraction at volume 13, then the LV dilates (diastolic phase) up to the volume 22 and starts contracting again (systolic phase).

and subjected to midline sternotomy to expose the heart. The spatial resolution for envelope-detected images in spherical coordinates was $384 \times 62 \times 56$, with 24 volumes per sequence on average. For the given temporal resolution, the motion between the two consecutive images is small, and the correlated speckle assumption holds.

For every scan, we consecutively register 3D images one onto the previous, starting from the first two images. We model the transformation \mathcal{T} using the Free Form Deformation (FFD) [23] with regularization. We put the FFD control points uniformly with 10 voxels spacing. The transformation estimated in spherical coordinates were then converted to Cartesian coordinates. For the comparison we used the SSD , CD_2 , MS and MS_2 similarity measures. We set $D = 1$, $\rho = 0.8$ and $m = 0.5$, which we empirically found to give the best performance. We implemented the algorithm in Matlab, and tested on a Pentium4 CPU 3GHz with 4GB RAM. On average, the tracking algorithm between two volumes requires around 10 minutes. The computational time can be significantly reduced, for instance, using the dedicated implementation (e.g., in C++ instead of Matlab), parallel processing, optimization only around the myocardium, etc.

To visualize the LV motion, we also pre-aligned the endocardium and epicardium contours, and found their motion (displacement field) [2]. Figure 3 shows the estimated motion of LV endocardium, epicardium contours and sonomicrometers. Figure 4(a,b) shows the displacement vector field visualized at the LV endocardium position between end diastole and end systole volumes at different viewing angles.

For validation, we computed correlation coefficients (CC) between algorithm- and sonomicrometry-derived strains and twists, which were averaged over all

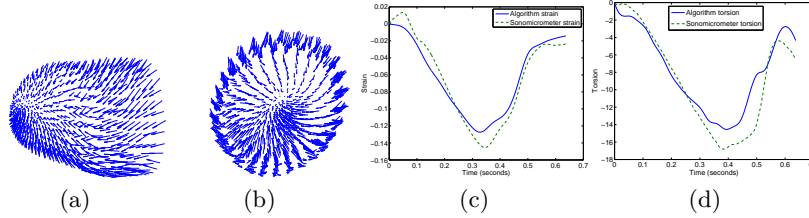


Fig. 4. (a,b) The displacement vector fields on LV endocardium between end diastole and end systole volumes at two different viewing angles. (c) A comparison between the algorithm- and sonomicrometry-derived measures. Strain between a single pair of crystals through time. (d) Torsion between the apex and base planes (in degrees).

pairs (for strain) and across all volumes of all piglets. Figure 4(c,d) illustrates a typical strain plot between a single pair of crystals and a typical twist (in degrees) during the cardiac cycle. The average CC achieved with SSD , CD_2 , MS and MS_2 is shown in the table.

| | SSD | CD_2 | MS | MS_2 |
|-----------|-------------------|-------------------|-------------------|-------------------|
| strain CC | 0.882 ± 0.053 | 0.913 ± 0.018 | 0.927 ± 0.021 | 0.929 ± 0.019 |
| twist CC | 0.934 ± 0.026 | 0.951 ± 0.012 | 0.958 ± 0.010 | 0.961 ± 0.012 |

On average, MS and MS_2 outperform both SSD and CD_2 similarity measures, which demonstrates their accuracy in ultrasound image registration.

5 Discussion and Conclusion

We present a method for automated processing of 3D echo images, which includes two main contributions: a) we introduce a new similarity measure for sequential non-rigid registration of ultrasound images, derived from the maximum likelihood perspective, b) we register images in spherical coordinate system instead of Cartesian coordinates.

The MS and MS_2 similarity measures explicitly considers the correlated speckle noise between the consecutive frames, its formation and acquisition process in ultrasound imaging. We use sonomicrometry to validate the algorithm. We found a strong correlation, between the algorithm- and sonomicrometry-derived strain and twist. The new similarity measures demonstrated accurate and robust performance compared to other similarity measures.

Image processing in raw spherical coordinates benefits from high resolution in axial direction without the interpolation artifacts resulted from conversion to Cartesian coordinates. The pre-converted data preserves speckle statistics, modeled for ML estimation. Finally, the conversion to the Cartesian system of a single 3D images, even by sacrificing the half of axial resolution, takes several magnitudes more operative memory, which greatly slows down the processing. Thus, processing the images directly in raw spherical format before conversion benefits both in resolution and computation speed.

References

1. Lang, M., Mor-Avi, V., Sugeng, L., Nieman, P., Sahn, D.J.: Three-dimensional echocardiography. *Jour. of the Am. Coll. of Cardiology* **48**(10) (2006) 2053–2069
2. Myronenko, A., Song, X., Sahn, D.J.: LV motion tracking from 3D echocardiography using textural and structural information. In: MICCAI. Volume 4792 of *Lecture Notes in Computer Science.*, Springer (2007) 428–435
3. Elen, A., Choi, H.F., Loeckx, D., Gao, H., Claus, P., Suetens, P., Maes, F., D’hooge, J.: Three-dimensional cardiac strain estimation using spatio-temporal elastic registration of ultrasound images: A feasibility study. *TMI* **27**(11) (2008) 1580–1591
4. Leung, K., van Stralen, M., Nemes, A., Voormolen, M., van Burken, G., Geleijnse, M., J., t., Reiber, J., de Jong, N., van der Steen, A., Bosch, J.: Sparse registration for 3D stress echocardiography. *Medical Imaging* **27**(11) (2008) 1568–1579
5. Ledesma-Carbayo, M., Kybic, J., Desco, M., Santos, A., Sühling, M., Hunziker, P., Unser, M.: Spatio-temporal nonrigid registration for ultrasound cardiac motion estimation. *IEEE Transactions on Medical Imaging* **24**(9) (2005) 1113–1126
6. Sanchez-Ortiz, G., Wright, G., Clarke, N., Declerck, J., Banning, A., Noble, J.: Automated 3-d echocardiography analysis compared with manual delineations and spect muga. *IEEE Transactions on Medical Imaging* **21**(9) (2002) 1069–1076
7. Cohen, B., Dinstein, I.: New maximum likelihood motion estimation schemes for noisy ultrasound images. *Pattern Recognition* **35**(2) (2002) 455–463
8. Cobbold, R.S.C.: *Foundations of Biomedical Ultrasound*. Biomedical Engineering Series. Oxford University Press (2006)
9. Burckhardt, C.B.: Speckle in ultrasound b-mode scans. *IEEE Trans. on Sonics and Ultrasonics* **25**(1) (1978)
10. Meunier, J.: Tissue motion assessment from 3d echographic speckle tracking. *Physics in medicine and biology*. **43**(5) (1998) 1241–1254
11. Goodman, J.W.: *Speckle Phenomena in Optics. Theory and Applications*. (2006)
12. Chandrashekar, R., Mohiaddin, R.H., Rueckert, D.: Daniel rueckert. In: *Surgery Simulation and Soft Tissue Modeling*. Volume 2673 of *LNCS*. (2003) 88–99
13. Roche, A., Malandain, G., Ayache, N.: Unifying maximum likelihood approaches in medical image registration. *IJIST* **11** (2000) 71–80
14. Papoulis, A.: *Probability, Random Variables, and Stochastic Processes*. (1991)
15. Boukerroui, D., Noble, J.A., Brady, M.: Velocity estimation in ultrasound images: A block matching approach. *IPMI* **2732** (2003) 586–598
16. Revell, J., Mirmehdi, M., McNally, D.: Combined ultrasound speckle pattern similarity measures. In: *MIUA, BMVA Press* (2004) 149–153
17. Song, X., Myronenko, A., Sahn, D.J.: Speckle tracking in 3D echocardiography with motion coherence. In: *Comp. Vision and Patt. Recognition (CVPR)*. (2007)
18. Linguraru, M.G., Vasilyev, N.V., Marx, G.R., Tworetzky, W., Nido, P.J.D., Howe, R.D.: Fast block flow tracking of atrial septal defects in 4D echo. *MIA* (2008)
19. Sloane, N.: Online enc. of integer sequences. A002457,A002802,A020918. (2008)
20. Miller, K., Bernstein, R., Bluemenson, L.: Generalized rayleigh processes. *Quarterly of Applied Mathematics* **16** (1958) 137–145
21. Shankar, P.M.: A general statistical model for ultrasonic backscattering from tissues. *IEEE T. Ultr., Ferr. and Frequency Control* **47**(3) (2000) 727–736
22. Tan, C.C., Beaulieu, N.C.: Infinite series representations of the bivariate rayleigh and nakagami-m distributions. *IEEE Trans. Communications* **45**(10) (1997)
23. Rueckert, D., Sonoda, L.I., Hayes, C., Hill, D.L.G., Leach, M.O., Hawkes, D.J.: Nonrigid registration using free-form deformations: Application to breast MR images. *IEEE Trans. Image Processing* **18**(8) (1999) 712–721